RESEARCH ARTICLE | SEPTEMBER 09 2025

# A new true triaxial apparatus with pore fluid system for rock deformation under representative crustal stress conditions

Ashley Stanton-Yonge ; Thomas M. Mitchell ; Philip G. Meredith ; Neil Hughes ; Steve Boon ; John Browning ; David Healy ; John Bowles



*Rev. Sci. Instrum.* 96, 095205 (2025)
https://doi.org/10.1063/5.0274588

Review of Scientific Instruments ARTICLE pubs.aip.org/aip/rsi

# A new true triaxial apparatus with pore fluid system for rock deformation under representative crustal stress conditions

Cite as: Rev. Sci. Instrum. 96, 095205 (2025); doi: 10.1063/5.0274588
Submitted: 7 April 2025 • Accepted: 16 August 2025 •
Published Online: 9 September 2025



Ashley Stanton-Yonge,[1,2,a)] Thomas M. Mitchell,[2] Philip G. Meredith,[2] Neil Hughes,[2] Steve Boon,[2] John Browning,[2,3] David Healy,[4] and John Bowles[2]

## AFFILIATIONS

[1] Department of Geosciences, University of Padua, Padova, Italy
[2] Department of Earth Sciences, University College London, London, United Kingdom
[3] Department of Structural and Geotechnical Engineering, Pontificia Universidad Católica de Chile, Santiago, Chile
[4] Geosolutions, School of Earth and Environment, University of Leeds, Leeds, United Kingdom

[a)] Author to whom correspondence should be addressed: ashley.stantonyongesesnic@unipd.it

## ABSTRACT

We have developed a new true triaxial apparatus for rock deformation, featuring six servo-controlled loading rams capable of applying maximum stresses of 220 MPa along the two horizontal axes and 400 MPa along the vertical axis to cubic rock samples of 50 mm side. Samples are introduced into a steel vessel, allowing rock specimens to be subjected to confining pressures of up to 60 MPa. Pore fluid lines connected to two pump intensifiers enable high-precision permeability measurements along all three principal stress directions. Experiments are conducted at room temperature. We present a suite of finite element method models implemented to determine the conditions and loading configuration that minimize the loading boundary effects during true triaxial loading. These observations are generic, and we expect they will contribute to the development of true triaxial loading systems generally. Finally, we validate our experimental configuration by presenting results on permeability measurements along the three axes on cubic samples of three types of well-studied rocks: Darley Dale sandstone, Crab Orchard sandstone, and Etna basalt.





## I. INTRODUCTION

The general state of stress in the crust is triaxial (Zoback *et al.*, 2003). In consequence, rocks experience deformation and eventual failure under the influence of three unequal principal stresses acting along mutually orthogonal orientations, denoted as $\sigma_1$, $\sigma_2$, and $\sigma_3$, and with $\sigma_1 > \sigma_2 > \sigma_3$. Despite this, the vast majority of rock deformation experiments have typically been conducted under axisymmetric (or conventional triaxial) loading configurations, consisting of cylindrical rock specimens subjected to a confining pressure plus an axial stress. Due to its versatility and relative ease of use, the conventional triaxial test constitutes one of the most widespread experimental procedures in rock deformation studies. However, this configuration disregards the effect of $\sigma_2$ on the physical and deformation properties of rocks, thus limiting the extrapolation of results to representative crustal conditions.

Building on early experiments by Kármán (1911) and Boker (1915), and aiming to investigate the influence of the intermediate principal stress ($\sigma_2$) on rock strength, Murrell (1965) and Mogi (1967) independently conducted conventional triaxial tests using the two standard loading configurations permitted by the method: the compressive test ($\sigma_1 > \sigma_2 = \sigma_3$) and the extension test ($\sigma_1 = \sigma_2 > \sigma_3$). These studies consistently revealed a disparity between the failure envelopes for various rock types under the two loading conditions, demonstrating that increased $\sigma_2$ relative to $\sigma_3$ enhances rock strength. Supporting findings were reported by Handin *et al.* (1967), who conducted pioneering experiments involving truly triaxial stress states by applying combined compression and torsion to hollow cylindrical rock specimens.

Since then, multiple efforts have been conducted to design and implement a rock deformation apparatus to allow for independent control of three loading axes (Takahashi and Koide, 1989; Mogi, 2006; Li *et al.*, 2012), the so-called True Triaxial Apparatus (TTA). Takahashi *et al.* (2001) established three categories of TTA, depending on the loading method. The rigid platen TTA (Furuzumi and Sugimoto, 1986; Esaki and Kimura, 1989; King *et al.*, 1997; Skoczylas and Henry, 1995; Sibai *et al.*, 1997; Alexeev *et al.*, 2004; Tiwari and Rao, 2004; Cheon *et al.*, 2006; He *et al.*, 2010; Tshibangu and Descamps, 2012; Rukhaiyar and Samadhiya, 2017; Zheng *et al.*, 2024) consists of three or six load rams transmitting stresses to a cubic or prismatic rock specimen through rigid platens. This configuration allows for high loading capacities and testing specimens with large dimensions. However, the installation of three or six loading rams with an appropriately stiff reaction ring and loading frame makes this design considerably complex and expensive. In addition, the rigid platen configuration induces loading boundary effects that may cause significantly heterogeneous stress distributions within the sample. First, the stiffness contrast between the rock sample and the rigid platens generates radial shear forces at the rock–platen interface, causing a clamping effect within a region at the edges of the sample (Mogi, 1967; Hawkes and Mellor, 1970). Second, the requirement that loading platens must necessarily be slightly smaller than the rock specimen results in unstressed sample edges that may cause significant stress concentrations (Shi *et al.*, 2012).

In contrast, the flexible medium TTA (Atkinson and Ko, 1973; Michelis, 1988; Smart, 1995) achieves genuinely triaxial stress states in rock samples by using fluid pressure along two or three loading axes. Loads are transmitted uniformly to the surfaces of the rock sample through flexible cushions. This design allows for homogeneous stress distributions in the sample, effectively avoiding unstressed edges and friction end effects. However, the loading capacity of such designs is usually not sufficient for studying rock deformation under high stress and failure.

A third type of TTA, initially developed by Mogi (1971) and thereafter adapted in several laboratories (Spetzler *et al.*, 1981; Takahashi and Koide, 1989; Wawersik *et al.*, 1997; Haimson and Chang, 2000; Lombos *et al.*, 2012; Feng *et al.*, 2016; Shi *et al.*, 2017), employs the rigid platen method to load the sample in the $\sigma_1$ and $\sigma_2$ directions and a fluid confining medium for $\sigma_3$. This configuration can achieve high loads, and by applying $\sigma_3$ homogeneously, loading boundary effects are reduced (Mogi, 2006). In addition, because the design already contemplates subjecting the sample to confining pressure, the introduction of a pore fluid system to allow for the deformation of saturated rocks and the measurement of permeability is relatively simple. However, this configuration poses additional challenges, such as the isolation of the rock specimen from the confining medium.

In addition, TTAs exclusively dedicated to the study of hydraulic fracturing under true triaxial conditions have recently been developed (Huang *et al.*, 2011; Frash *et al.*, 2014; Muñoz-Ibáñez *et al.*, 2019), as well as an apparatus dedicated to ice deformation under true triaxial conditions (Golding, 2012).

The number of TTA constructed in laboratories has vastly increased during the past decades, as well as the volume of collected data. Although advances in standardizing the procedures for true triaxial rock deformation tests have been made (Feng *et al.*, 2019), significant issues still remain regarding the repeatability and generalization of the results. For example, even though numerous studies have supported the dependence of rock strength on $\sigma_2$, no general consensus on the form of this dependence has been reached (Paterson and Wong, 2005; Kwaśniewski, 2012; Xie *et al.*, 2022). Furthermore, with some exceptions (Lombos *et al.*, 2012; Shi *et al.*, 2017), the vast majority of the implemented TTAs do not consider a pore fluid system and can only deform dry rock samples. As a result, there is currently an important gap in our knowledge of the deformation of saturated rocks and their fluid flow properties under representative crustal stress conditions.

In order to study the deformation and failure of rocks under true triaxial conditions, the design and manufacture of a new apparatus was commissioned at the Rock and Ice Physics Laboratory of UCL in 2002. In its initial design, the apparatus consisted of a pressure vessel and four double acting actuators ("X" and "Y" axes) located in the vessel wall to load a square section rock specimen within the pressure vessel, plus two additional actuators at the bottom and top of the vessel to provide axial load along the Z axis. The original conceptualization of this apparatus included two different operating modes: (1) using $30 \times 30 \times 75$ mm$^3$ prismatic samples, and (2) using $50 \times 50 \times 50$ mm$^3$ cubic samples. The prismatic sample arrangement was envisioned to examine true triaxial deformation and failure using the normal 2.5 to 1 length to width ratio needed for strength and failure measurements. The cubic sample arrangement was designed to investigate the evolution of the crack damage envelope under true triaxial loading conditions, as reported by Browning *et al.* (2017) and Browning *et al.* (2018), but under saturated and elevated pore fluid pressure conditions, that is, under conditions more relevant to those at depth in the Earth's crust.

A major challenge of deformation experiments on cubic rock samples loaded through six pistons and under pressurized pore fluid conditions is the sealing of the samples' exposed edges. A jacket system is needed to isolate the pressurized pore fluids within the sample from the confining medium, a challenging feat due to the sharp edges of the cubic sample. The initial concept of UCL's TTA was to address this issue by dispensing with edge seals altogether and to saturate and pressurize the sample with the fluid inside the pressure vessel (water or brine). Since this initial concept, the system has evolved through the introduction of an edge sealing system and two fluid pressure pumps that allow for the contemporaneous measurement of fluid flow across the sample while it is being deformed under true triaxial conditions.

In its current form, the TTA instrument manufactured in UCL consists of six servo-controlled loading rams that transmit maximum stresses of 220 MPa along the two horizontal axes and 400 MPa along the vertical axis to 50 mm side cubic rock samples through rigid platens. The sample and loading platen assembly are located inside the steel pressure vessel, where rock specimens can be subjected to up to 60 MPa of confining pressure provided by silicone oil. Pore fluid lines are installed along the three loading axes, which are connected to two pump intensifiers that allow for highly accurate permeability measurements to be made by means of the steady-state flow method.

To accurately simulate crustal conditions, the rock deformation apparatus should be capable of operating under elevated temperature conditions. Although some TTAs have been constructed with this capability (Kern, 2011; Lombos *et al.*, 2012; Frash *et al.*, 2014), high temperature deformation tests are not currently

possible with the UCL TTA configuration. Incorporating a furnace to heat the sample and a pressure vessel introduces additional challenges, such as potential misalignments in the sample assembly due to the thermal expansion of individual components. As a result, the apparatus described here is presently limited to room-temperature experiments.

The present article is organized as follows: We first describe the implementation and design of UCL's TTA with details of materials and specifications for the mechanical design and hydraulic control. Next, we present a suite of Finite Element Method (FEM) models implemented to determine the conditions and loading configuration that minimizes loading boundary effects during true triaxial loading. These observations are generic, and we, therefore, expect they will contribute to the development of true triaxial loading systems generally. Finally, we validate our experimental configuration by presenting results on permeability measurements along the three axes of cubic samples of three types of well-studied rocks: Darley Dale Sandstone (DDS), Crab Orchard Sandstone (COS), and Etna Basalt (EB).

## II. DESIGN AND IMPLEMENTATION OF THE TRUE TRIAXIAL APPARATUS

The true triaxial apparatus (TTA) was custom-designed and fabricated in-house at University College London. Its design meets the demanding requirements of multi-axial rock deformation experiments under representative crustal stress conditions, enabling precise independent control of load along three orthogonal axes and integration of pore pressure and confining systems. The pressure vessel and primary structural elements are constructed from super duplex stainless steel (UNS S32760, F55), selected for its high yield strength, excellent corrosion resistance, and mechanical durability under confining pressures up to 60 MPa. High-pressure pistons, caps, and load-transmitting platens are machined from FV520B precipitation-hardened stainless steel, offering superior tensile strength and fatigue resistance in cyclic loading applications. Actuator housings, piston rods, reaction ring assemblies, and structural supports are produced from EN24T high-tensile alloy steel and EN8 medium carbon steel, ensuring mechanical robustness and resistance to fatigue. All corrosion-sensitive fittings, couplings, and hydraulic connections are fabricated from stainless steel grades 316, 304, or 303, while non-load-bearing components such as platforms, jigs, and alignment fixtures are made from aluminum alloys for weight reduction without compromising system rigidity. Each hydraulic actuator is a double-acting design, allowing controlled extension and retraction under servo control. The actuators are arranged in mechanically opposed pairs along each axis ($X_1/X_2$, $Y_1/Y_2$, and $Z_1/Z_2$), ensuring that applied forces are balanced and that side loads on the sample and frame are minimized. This configuration reduces hydraulic drift and enhances load stability during multi-axial loading. The reaction frame, constructed as a modular split assembly, integrates with a 1500 kN capacity servo-hydraulic load frame. The system is capable of applying independent maximum stresses of 400 MPa on the vertical (Z) axis and 220 MPa on each horizontal (X and Y) axis, transmitted through rigid platens to 50 mm cubic rock samples held within the pressure vessel. The reaction frame, constructed as a modular split assembly, integrates with a 1500 kN capacity servo-hydraulic load frame (Fig. 1). The system is capable of applying independent maximum stresses of 400 MPa on the vertical (Z) axis and 220 MPa on each horizontal (X and Y) axis,

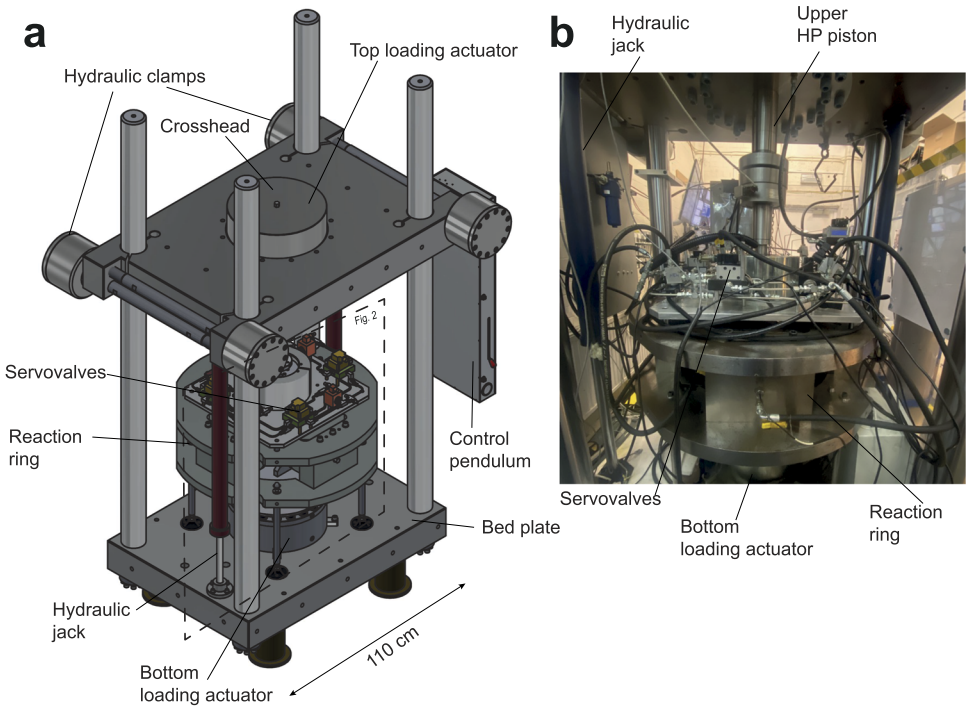


**FIG. 1.** (a) 3D view of the TTA load frame and reaction ring. The dashed rectangle indicates the section displayed in Fig. 2. (b) TTA cell.

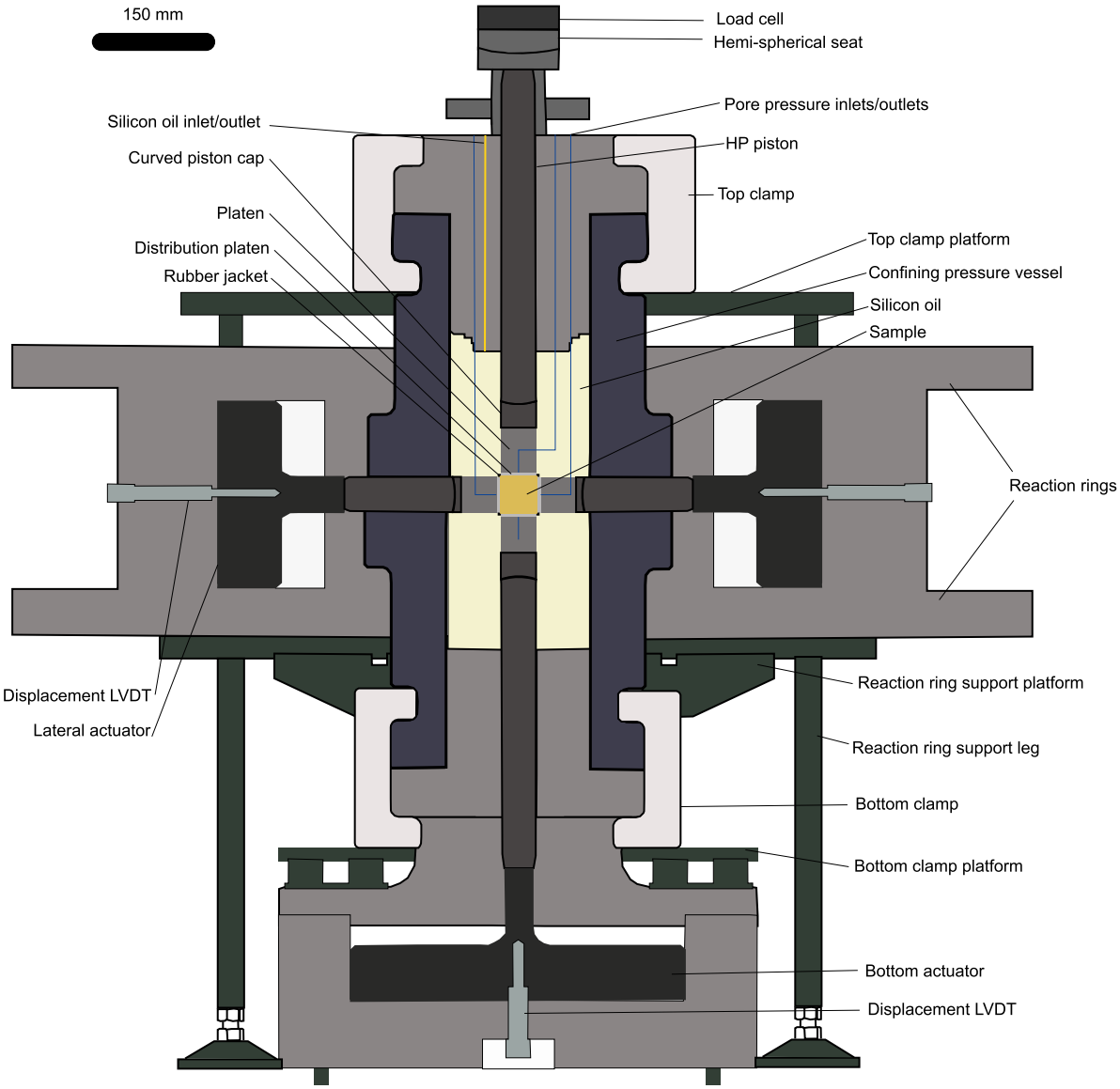


**FIG. 2.** Section view of UCL's TTA cell, with labeled constitutive parts.

transmitted through rigid platens to 50 mm cubic rock samples held within the pressure vessel. A section of the pressure vessel, actuators, and reaction ring is shown with the corresponding constitutive parts in Fig. 2.

### A. Hydraulic servo control system and signal conditioning

Hydraulic control is achieved using Star Hydraulics 550-series two-stage flapper-nozzle electrohydraulic servovalves, each paired with a Star STE3900-15 servo amplifier. These valves provide precise flow control at system pressures up to 350 bars, with a dynamic frequency response of 80–150 Hz and hysteresis below 1%, enabling responsive and accurate load application and feedback control. The STE3900-15 amplifiers deliver ±10 V control signals with adjustable gain, bias, and damping, driven by the National Instruments PXI-based rock deformation control system (RDCS). The RDCS manages multi-axis proportional integral derivative (PID) control, real-time data acquisition at sampling rates up to 1000 Hz, programmable ramp and hold functions, and integrated safety interlocks. All sensors, including load cells, pressure transducers, potentiometers, and linear variable differential transformers (LVDTs), are signal-conditioned through RDP Electronics amplifier modules and a custom multi-channel amplifier board. This setup provides precision gain adjustment, zeroing, and signal filtering, ensuring

stable and accurate input to both control loops and data acquisition systems.

### B. Hydraulic axis control, fast-acting solenoids, and displacement measurement

Each hydraulic axis is fitted with an inline hydraulic solenoid valve on the pressure side of the actuator. These solenoids, controlled by the RDCS, allow rapid hydraulic isolation of each ram, enabling precise piston positioning, minimization of drift, and load stabilization during static holds or incremental loading. The system allows seamless transition between dynamic servo-controlled loading and hydraulic isolation, supporting both rapid load cycling and fine, stable control during sensitive experimental stages. Ram displacement on all six actuators is continuously monitored using Penny and Giles ICS100 series in-cylinder linear displacement transducers. The X and Y axis cross-bore actuators are each equipped with ICS100/EM/115/H/01 sensors, while the top and bottom Z-axis actuators use ICS100/EM/60/H/01 sensors. These hybrid-track potentiometric transducers offer ±0.15%–0.25% linearity, virtually infinite resolution (practically limited to less than 0.01 mm), and reliable operation under hydraulic pressures up to 50 MPa. The analog voltage output is conditioned through RDP Electronics amplifiers and integrated into the RDCS, allowing real-time feedback control of piston displacement. The in-cylinder mounting design ensures precise, maintenance-free measurement, critical for fine control of actuator position during triaxial testing. A schematic diagram illustrating the servo-controlled and solenoid system for hydraulic axis control is displayed in Fig. 3.

### C. Load measurement on X, Y, and Z axes

The TTA applies independently controlled loads along three orthogonal axes, each monitored by dedicated measurement systems suited to the apparatus geometry. Vertical loads (Z-axis) are measured using a low-profile compression load cell (RDP SLC060P44201) rated to 1780 kN (400 000 lbs), with a linearity and hysteresis of ±0.20% full scale (FS). The load cell is factory-calibrated to international standards and continuously monitored by the RDCS for feedback control. Horizontal loads (X and Y axes) are monitored using Applied Measurements PR3200 wet/wet differential pressure transducers. These sensors measure pressure differences across each hydraulic ram's power and return lines and are calibrated to correlate directly with applied load. The PR3200 sensors offer linearity and hysteresis better than ±0.25% FS and were selected based on the hydraulic circuit's operating ranges.

All transducers were first calibrated *in situ* using a custom-built compression load cell placed between opposing rams inside the pressure vessel. This procedure accounts for system compliance, hydraulic friction, and seal effects, yielding a load measurement accuracy of ±2% of applied load post-calibration.

In addition, the voltage outputs of the pressure transducers were calibrated to load by applying sequential confining pressure steps with all the pistons located inside the vessel, but with no sample or sample assembly present. This allowed us to compare the outputs from the differential pressure transducers with the load that is theoretically being applied to each piston ($L_{theo}$), calculated as $L_{theo} = P_c A_p$, where $P_c$ is the confining pressure and $A_p$ the cross sectional area of the piston (Fig. 4).

### D. Stiffness calibration and system compliance

To quantify the mechanical compliance of the apparatus under load and assess the contribution of frame, actuator, and vessel deformation to the measured displacements, we performed a dedicated stiffness calibration using custom-machined steel calibration samples. Two 50 mm cubes were fabricated from EN24T steel (817M40), a material with a Young's modulus of 210 GPa, a yield stress of



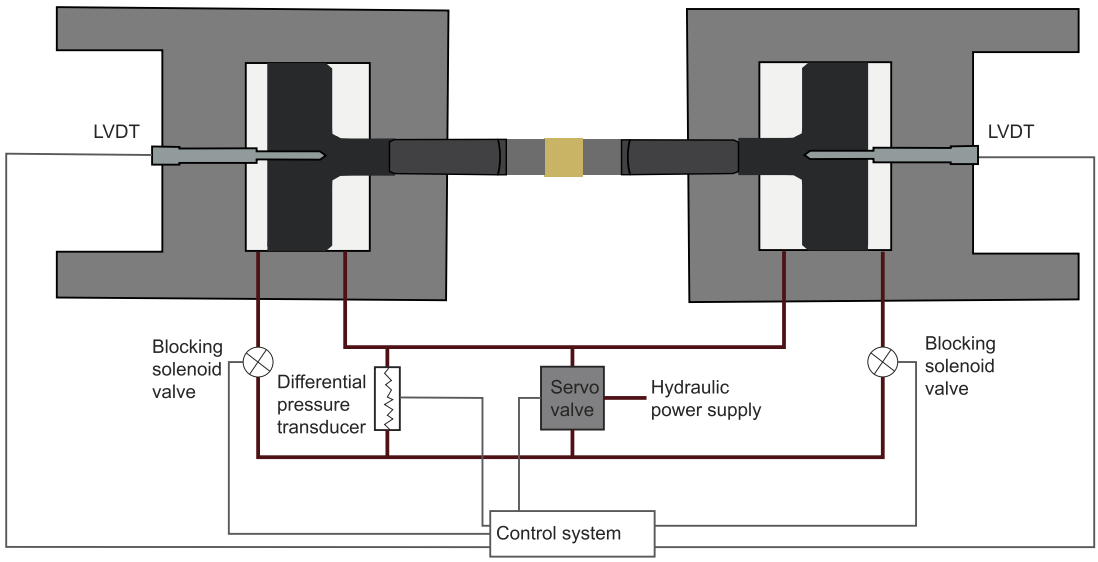


**FIG. 3.** Schematic diagram of one loading axis indicating the hydraulic axis control, fast-acting solenoids, and displacement measurement.

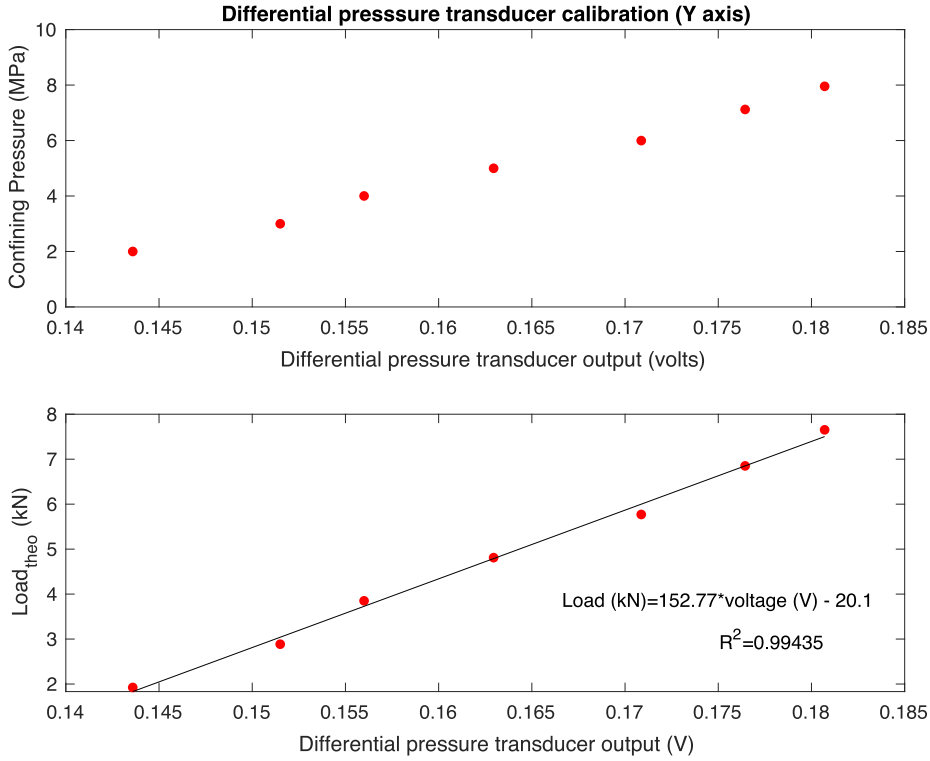


**FIG. 4.** Calibration of the differential pressure transducer for load reading along the Y axis.

680–665 MPa, and a hardness of 248–302 Brinell in the T condition. These cubes were jacketed using the same procedure as for rock specimens and mounted within the apparatus. Calibration tests were conducted by applying load simultaneously along all three principal axes under confining pressure while recording piston displacements with the in-cylinder displacement sensors. This procedure allowed us to determine the global stiffness of the apparatus separately along the X, Y, and Z axes. Due to the symmetric configuration of the X and Y loading systems, these axes exhibit comparable stiffness values, while the Z-axis, supported by the external load frame, presents a distinct stiffness characteristic. The measured stiffness values—164 kN/mm for X and Y and 206 kN/mm for Z—are used to correct for system compliance in experimental data analysis, ensuring accurate interpretation of displacement and strain measurements.

### E. Pressure intensifier system and measurement

Confining pressure and pore fluid pressures are controlled by three custom-built hydraulic intensifiers, each operated via a Star 550-series servovalve. The intensifiers incorporate high-pressure pistons sealed with step seals, designed for durability under repeated high-pressure cycles. Piston displacement is monitored by Penny and Giles SLS095 linear potentiometers, providing ±0.15%–0.5% linearity with an effective resolution of ~0.005 mm. This allows for precise measurement of piston displacement and calculation of fluid volume. Pressure is monitored by Applied Measurements P6010FAC transducers, rated to 200 MPa with ±0.25% FS accuracy. The intensifiers can be operated in either pressure-controlled or volume-controlled mode, with control seamlessly managed by the RDCS software. This allows precise regulation of pore pressure and confining pressure for deformation and permeability experiments.

The confining pressure system employs silicone oil as the hydraulic medium, in line with standard practice across all high-pressure equipment in the UCL Rock and Ice Physics Laboratory. Although experiments are conducted at room temperature, silicone oil was selected for its superior pressure stability, low compressibility, and consistent viscosity under minor temperature fluctuations—characteristics that help minimize confining pressure drift during long-duration tests. Silicone oil also offers better compatibility with elastomeric seals and other sensitive components compared to mineral oils, reducing the risk of seal degradation and hydraulic contamination over repeated loading cycles. These factors make silicone oil a preferred choice in our laboratory environment, where stable, repeatable high-pressure operation is critical.

### F. Pore pressure system

Permeability ($k$) is measured by applying a pressure difference between the two pumps ($p_a$ and $p_b$) and allowing steady-state flow to develop along one of the three loading axes at a time. Two independent flow measurements ($Q$) are accurately taken by each intensifier, and permeability is calculated by applying Darcy's Law,

$$Q = \frac{-kA_s(p_b - p_a)}{\mu L}, \tag{1}$$

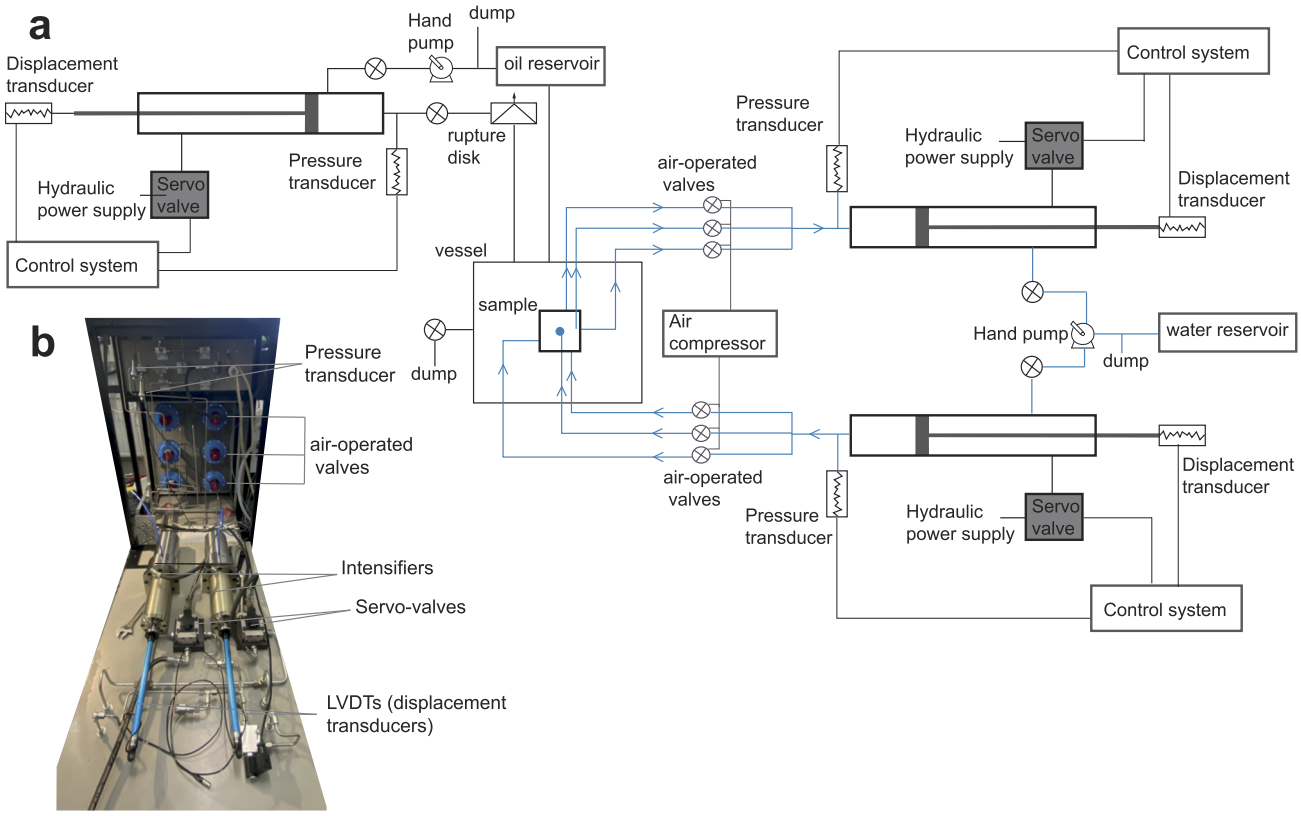


**FIG. 5.** (a) Schematic diagram of the confining pressure and pore fluid system. (b) Image of the pore fluid system with labeled constitutive parts.

where $A_s$ corresponds to the cross sectional area of the sample, $L$ is the sample length, and $\mu$ is the viscosity of the fluid. To avoid temperature induced permeability fluctuations, the room temperature is maintained constant at 21 ± 1 °C during all the experiments.

Once accurate flow measurements are obtained for a certain stress state along one loading axis, flow is interrupted along the recorded direction and is started along the next one. Pore fluid (distilled water) access is managed by six pneumatically actuated high-pressure valves (HIP 30-12HF4, normally closed), installed on each of the pore fluid lines for the six sample faces. These valves are actuated by air solenoids triggered by ±10 V signals from the RDCS, allowing for rapid, automated opening and closing of individual fluid pathways. This configuration supports fast switching during experiments, enabling sequential flow or injection protocols while maintaining high-pressure sealing and boundary condition integrity. The pore pressure and confining pressure systems are schematically illustrated in Fig. 5. An overall summary of the system's operational capacities is indicated in Table I.

**TABLE I.** Summary of the operational capacities of the apparatus.

| Feature | Specification |
|---|---|
| Maximum Z-axis load | 1780 kN (400 MPa) |
| Maximum X-axis/Y-axis load | 220 MPa |
| Maximum confining pressure | 60 MPa |
| Maximum pore pressure measurement | 200 MPa |
| Z-axis load cell accuracy | ±0.20% full scale |
| X-axis/Y-axis load measurement accuracy | ±2% of applied load (post-calibration) |
| Pressure transducer accuracy | ±0.25% full scale |
| Piston displacement resolution | 0.005 mm |
| Servo control response frequency | 80–150 Hz |
| Control system sampling rate | Up to 1000 Hz |

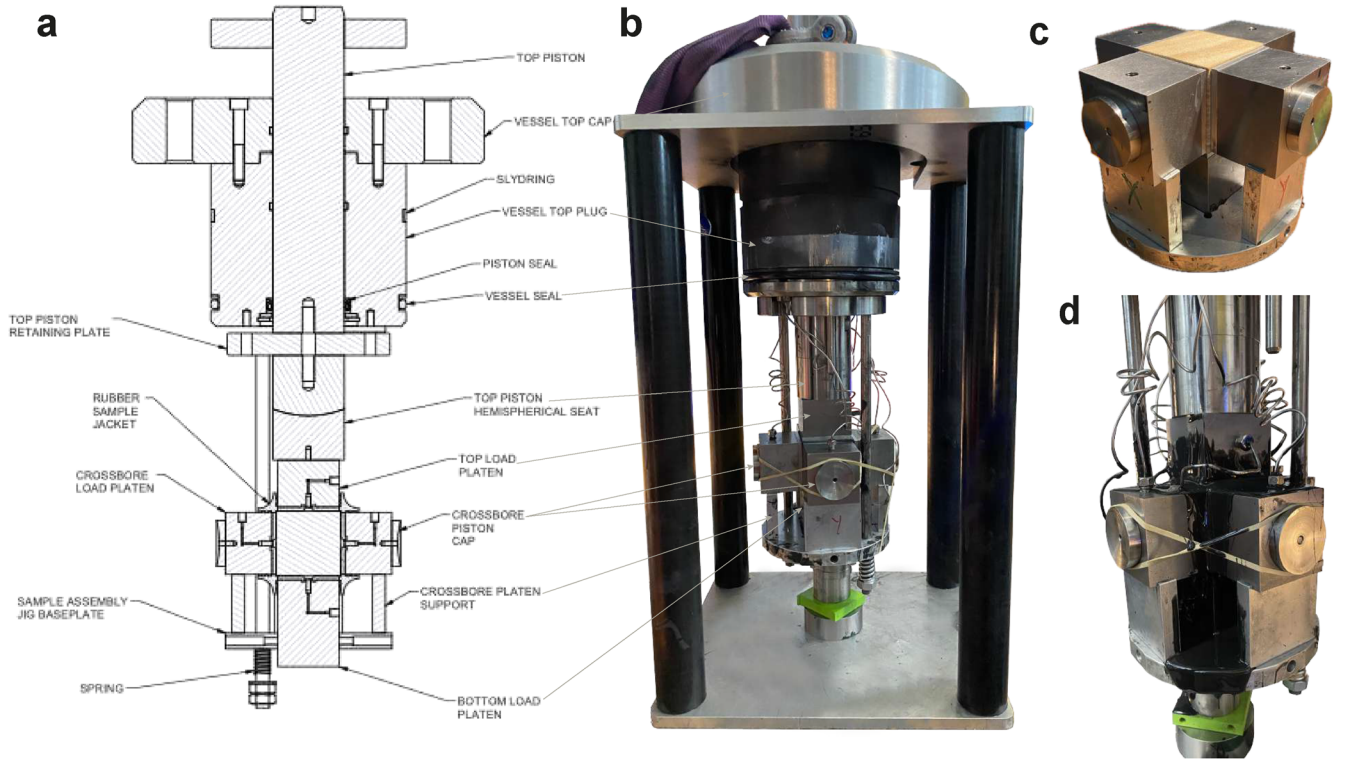


**FIG. 6.** (a) and (b) Sample assembly and vessel cap design, with labeled constitutive parts. (c) A cubic sample of Crab Orchard sandstone in an aluminum holder, prior to the manufacture of the rubber jacket, and without the upper loading platen. (d) Sample assembly with a cured rubber jacket sample.

### G. Sample assembly and jacketing system

Rock samples are saw cut and ground into cubes of 50 mm edge length with mutually orthogonal surfaces up to a tolerance of ∓0.01 mm by means of a high precision vise and square mounted on a surface grinder. The sample assembly was designed to ensure accurate alignment of the rock specimen throughout the experiments. A cross sectional view of the constituent parts of the vessel top plug, vessel cap, and sample assembly can be seen in Fig. 6(a). The sample jacket is made manually by applying several layers of liquid Polytek 74-29 flexible polyurethane rubber to the exposed edges of the sample, with each layer solidifying after a curing time of ~24 h [Fig. 6(d)]. The horizontal loading platens are held in their correct position by an aluminum holder. The bottom piston is kept in the same position throughout the experiments in order to ensure that the piston caps of the horizontal loading platens always remain aligned with the cross-bore pistons.

## III. FEM MODELS TO EVALUATE BOUNDARY EFFECTS DURING TRUE TRIAXIAL LOADING

Section III describes the implementation and results of a set of Finite Element Method (FEM) models designed to evaluate the effectiveness of practical measures that can be taken for reducing loading boundary effects in true triaxial rock deformation experiments. We explore the capability of platen material selection for reducing the end friction effect and the influence of confining pressure for decreasing the unstressed edges effect.

### A. Platen material selection for reducing end friction effect

The ideal conditions for rock deformation experiments require that stresses and deformation remain uniform across the loading planes at all times, with no shear stresses or distortion in the boundary planes (Hawkes and Mellor, 1970). However, using rigid pistons and platens (typically made of steel) to transmit stresses to rock specimens creates a stiffness mismatch between the rock and the metal. The resulting friction at the rock–platen interface leads to lateral restraint and radial shear forces, causing a clamping effect near the contact areas (Filon, 1902). This results in a heterogeneous stress distribution, which influences the measured mechanical properties of the rock samples. Stress concentrations can locally weaken the material, while fracture propagation is inhibited in the clamping region (Mogi, 2006).

It has been empirically shown that the use of a minimum height-to-diameter ratio of 2.5:1 for cylindrical samples effectively eliminates the influence of the end friction effect to measure the uniaxial compressive strength of rocks (Mogi, 1966). However, for true triaxial tests on cubic samples, not only is the sample geometry restricted to a 1:1 ratio, but shear stresses will also develop in each

of the four or six rock–platen interfaces, and these will potentially interact with each other.

Several scenarios have been proposed to reduce the end friction effect during such rock deformation experiments. Decreasing the platen–rock friction coefficient through the use of lubricants and/or Teflon sheets is a widely employed method (Shi *et al.*, 2012; Feng *et al.*, 2017). A significant problem with this method is the possibility of liquid or soft material intruding into the sample while being compressed, locally decreasing the effective stress and influencing the failure mode and strength of the tested materials (Mogi, 2006). The use of thin copper sheets can prevent that in some circumstances. However, the metal–Teflon–copper–rock configuration is impractical for experiments involving fluid flow across the sample due to the requirement for fluid to be evenly distributed across the rock faces to satisfy the assumptions of Darcy's Law.

An alternative method for reducing the end friction effect is to select a material for the loading platens that matches the elastic properties of the rock specimen as closely as possible. In the configuration of the UCL TTA [Figs. 2 and 6(a)], the rock–platen interface is between the sample and a thin platen used for fluid distribution across the sample face and is attached to the steel loading platen. We, therefore, use FEM models to explore the effect of selecting different materials (steel or aluminum) for the manufacture of the fluid distribution platens on the end friction effect developed when deforming a cubic sample of sandstone.

The models were implemented and run using the static structural module of the commercial software ANSYS. The model geometry is based on the drawings and 3D model developed during the design of UCL's TTA. The elastic properties of the materials are indicated in Table II. The rock sample and platen are modeled as rigid, linear elastic bodies, with a frictional contact between the rock sample and platen described by a static friction coefficient. We

**TABLE II.** Elastic properties of the materials considered for the FEM models.

| Material | E (GPa) | $\nu$ | Frictional contact coefficient |
|---|---|---|---|
| Sandstone | 35 | 0.2 | 0.2 |
| Steel | 210 | 0.3 | 0.2 |
| Aluminum | 77 | 0.33 | 0.2 |

deliberately chose not to consider the static friction coefficient as a variable in our simulations due to the difficulties associated with quantifying and controlling the rock–platen friction. In particular, our experimental setup does not allow for the use of standard friction-reducing methods (e.g., Teflon sheets or lubricants). Therefore, the friction coefficient is assumed to be equal for all interfaces.

Reliable measurements of static friction coefficients between rock and loading platens are scarce in the literature, with reported values varying significantly depending on rock type and measurement method. For our simulations, we selected a static friction coefficient of 0.2, which lies at the lower end of the range reported for unlubricated rock–platen interfaces by Hawkes and Mellor (1970). Feng *et al.* (2016) reported values ranging from 0.146 to 0.157 for unlubricated steel–granite interfaces, while Rashed and Peng (2015) reported a value of 0.25 for unlubricated steel–coal interfaces. These data suggest that a static friction coefficient of 0.2 is a reasonable and plausible choice.

To validate our model configuration, we first reproduce the end friction effect developed on a cylindrical sample of sandstone under uniaxial compression. This configuration has previously been analytically evaluated (Balla, 1960), allowing us to compare our results with those available from the literature (Fig. 7). Results are plotted in

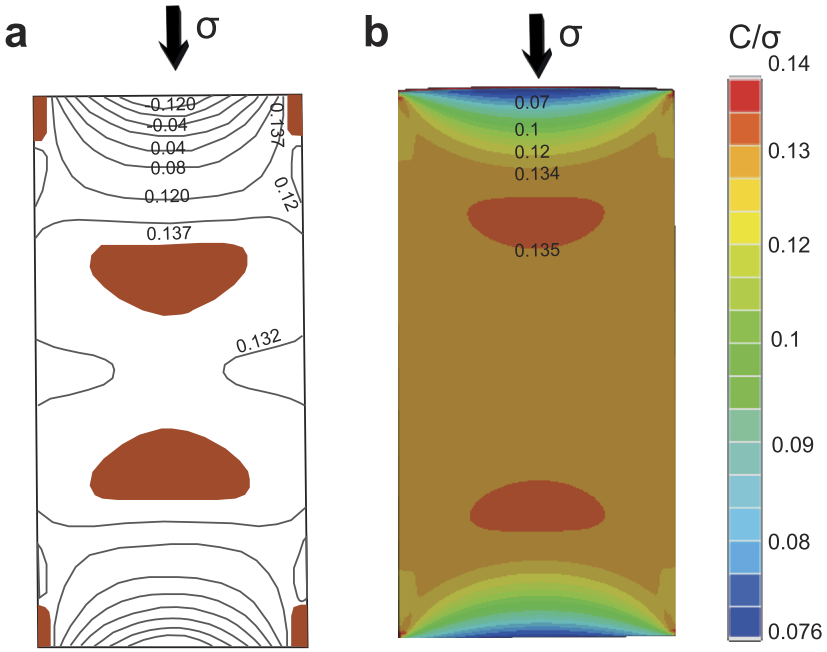


**FIG. 7.** (a) End friction effect in uniaxial compression of a cylinder, as plotted by Hawkes and Mellor (1970). Contours indicate the McClintock–Walsh failure criterion ($C$) normalized by the applied axial stress $\sigma$. Colored areas indicate the highly stressed regions where cracking is likely to initiate. (b) Results by our FEM model, with a colormap displaying $C$ normalized by the applied axial stress ($\sigma$ = 50 MPa).

the same form as Hawkes and Mellor (1970) [Fig. 7(a)], equivalent to the McClintock–Walsh failure criterion ($C$), normalized by the applied stress $\sigma$. $C$ is defined by

$$C = \frac{\sigma_1}{4}[(\mu^2+1)^{1/2} - \mu] - \frac{\sigma_3}{4}[(\mu^2+1)^{1/2} + \mu], \quad (2)$$

where $\sigma_1$ and $\sigma_3$ are the maximum and minimum principal stresses developed in the loaded sample, and $\mu$ is the internal friction coefficient of the rock (assumed to be 0.7). This failure criterion predicts that cracking will begin when $C$ surpasses the uniaxial tensile strength of the rock. Cracking and the highest crack density will, therefore, occur in the region of the sample where $C$ is the highest.

Our model results [Fig. 7(b)] reproduce the same features as those obtained by Balla (1960) and plotted by Hawkes and Mellor (1970). Mainly, a clamped, low stress region of half elliptical shape in the sample edges and stress concentrations (shaded/red areas) in the sample corners and in regions in between the clamped shadow and the sample center.

We then implement a similar model but with a sandstone sample of cubic shape, loaded through rigid steel pistons and fluid distribution platens of variable material [Fig. 8(a)]. Results are also presented as colormaps of the $C$ failure criteria normalized by the applied stress $\sigma$ [Figs. 8(b) and 8(c)]. The sample is loaded only along the vertical axis to visualize the effect of changing the platen material more clearly.

We observe that the use of aluminum platens, with a platen–rock stiffness ratio of $E_{platen}/E_{rock} = 2.1$, reduces the extent of the end friction effect with respect to using steel platens, $E_{platen}/E_{rock} = 5.9$, in that the clamped area is reduced, and the stress distribution within the remaining sample volume is considerably more homogeneous.

### B. Effect of confining pressure on reducing the unstressed edges effect

Another issue inherent to the true triaxial loading of cubic or prismatic rock samples arises from the requirement that the loading platens need to be slightly smaller than the rock sample to allow for the sample to deform while avoiding the rigid platens coming into contact with each other. The result of this configuration is that the edges of the samples remain unstressed throughout the experiments, which causes stress concentrations that have the potential to significantly influence the failure mechanism and strength of the tested materials (Shi *et al.*, 2012).

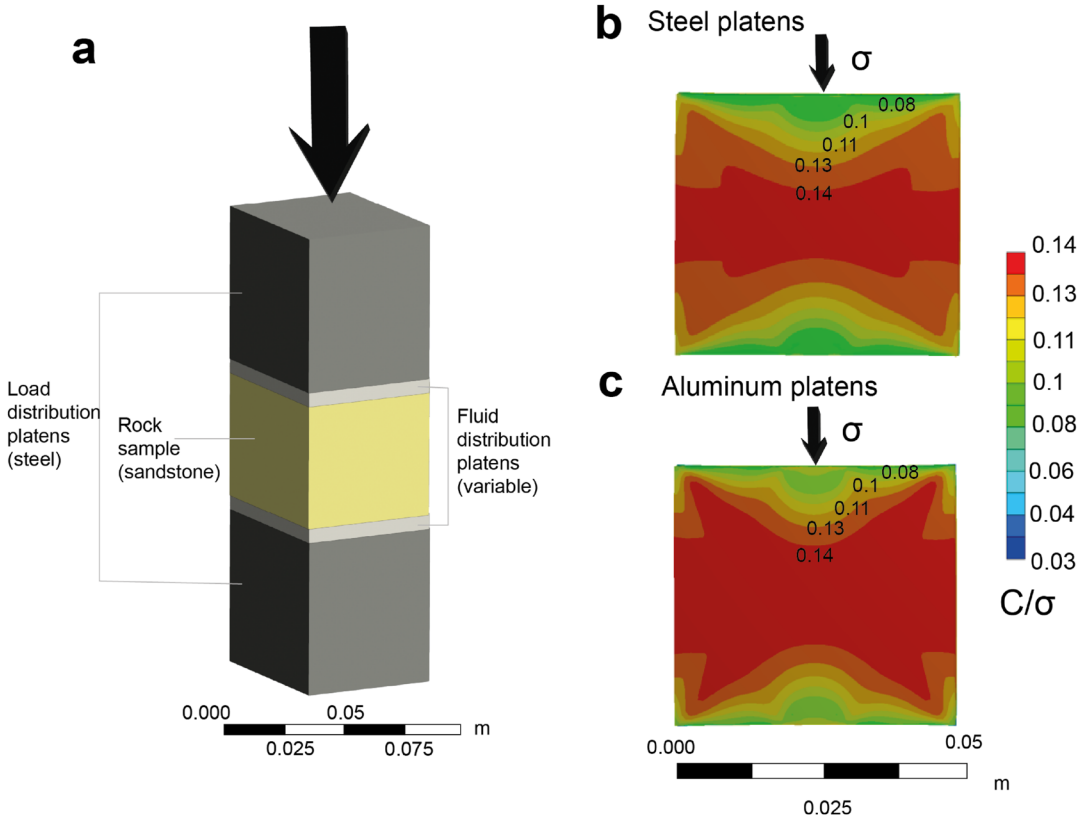


**FIG. 8.** (a) Configuration of the FEM model to evaluate the effect of platen material selection on the end friction effect of a cubic sample loaded uniaxially. (b) Stress distribution across a sample loaded through steel platens, plotted as the failure criterion $C$ normalized by the applied stress $\sigma$. (c) Stress distribution across a sample loaded through aluminum platens.

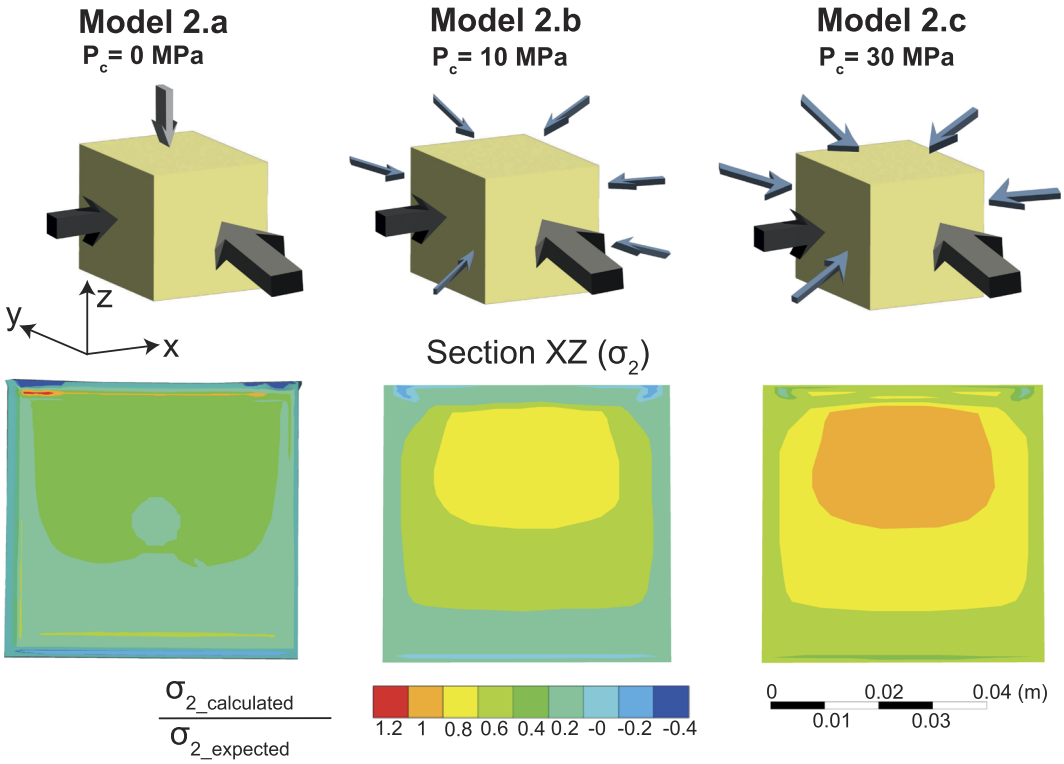


**FIG. 9.** Configuration and results of models implemented to quantify the effect of confining pressure on the reduction of stress concentrations due to the unstressed edge effect. Positive compressive stress convention is considered.

A potential advantage of the Mogi-type TTA with respect to the rigid platen TTA is that the confining medium should help reduce the stress concentrations caused by the unstressed edge effect (Mogi, 2006). However, the magnitude of this reduction as a function of the applied confining pressure remains unclear.

We, therefore, implemented a series of FEM models to quantify the effect that different magnitudes of confining pressure have on the stress concentrations produced by unstressed edges during true triaxial loading. To isolate this effect from other loading boundary effects (e.g., the end friction), the friction coefficient in the platen–rock interface was reduced to 0.1. All the modeled samples are subjected to a maximum stress ($\sigma_1$) of 100 MPa along the X-axis and an intermediate stress ($\sigma_2$) of 50 MPa along the Y-axis. The application of $\sigma_3$ varies in the different models. In model 2a (Fig. 9), a $\sigma_3$ of 10 MPa is applied through rigid platens along the Z-axis, whereas for models 2b and 2c, $\sigma_3$ is applied through a confining pressure of 10 and 30 MPa, respectively.

Results are plotted as the magnitude of $\sigma_2$ across the loaded samples calculated from the models, normalized by the expected magnitude of $\sigma_2$, along a cross section of the $\sigma_1/\sigma_3$ plane. Positive

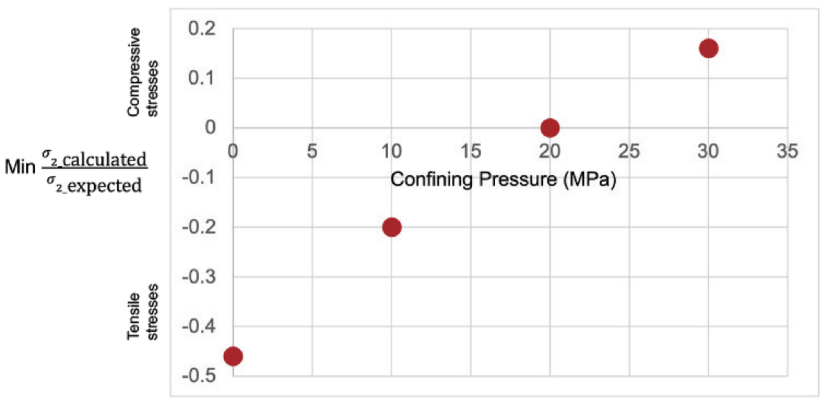


**FIG. 10.** Magnitude of the most stressed region of each model (negative magnitudes indicate tensile stresses) as a function of the confining pressure applied in the model.

compressive stress convention is used. A uniform distribution close to 1 would represent the ideal conditions for a true triaxial test. We observe that the application of a modest confining pressure ($P_c$) of 10 MPa (model 2b) significantly reduces the stress concentrations at the edges and corners with respect to the model where $P_c = 0$ (model 2a). The unstressed edges effect is almost completely eliminated by the application of $P_c = 30$ MPa (model 2c).

In order to clearly visualize the effect of $P_c$ on the stress concentrations produced by unstressed edges, the magnitude of the most stressed area (negative values representing tensile stresses) of each model is plotted against the modeled $P_c$ (Fig. 10). It can be observed that the tensile stressed regions normalized by the expected magnitude of $\sigma_2$ exhibit a linear relationship with the applied confining pressure and that a $P_c$ equal to 20 MPa eliminates tensile stresses in the unstressed regions. The projection of the linear trend indicates that increasing $P_c$ further to ~70 MPa would completely eliminate the unstressed edge stress concentrations by reaching a magnitude of calculated $\sigma_2$ normalized by expected $\sigma_2$ equal to 1.

## IV. EXPERIMENTAL VALIDATION

Cubic samples of three highly studied rocks—Darley Dale sandstone (DDS), Crab Orchard sandstone (COS), and Etna basalt (EB)—were introduced into UCL's TTA for triaxial permeability measurements under a hydrostatic confining pressure of 5 MPa (Fig. 11). Our results are consistent with previously reported permeability measurements for the studied rocks. The permeability of DDS under low hydrostatic pressure conditions ($<10MPa$) has been reported to be in the range of $10^{-14}$–$10^{-15}$ m$^2$ (Zhu and Wong, 1997), which is usually measured perpendicular to bedding (Z-axis in our study). Our results indicate the relatively isotropic permeability for our DDS sample, ranging from 2 to 2.6 $10^{-15}$ m$^2$. For the case of EB, Vinciguerra *et al.* (2005) report the permeability results on the order of $10^{-16}$ m$^2$ for low effective stresses. Although the orientation of the samples was not reported in the referenced study, the very low variability between P-wave velocity measurements taken for a variety of orientations suggested a high isotropy for the EB samples. Our permeability results on a cubic sample of EB indicate the highly isotropic permeability along the three axes, ranging from 8 to 9 $10^{-17}$ m$^2$. The results of COS are of particular interest, as a significant permeability anisotropy of 180% was reported between the directions parallel and orthogonal to the bedding (Gehne and Benson, 2017), with a bedding-parallel permeability of $k_x = 3 \times 10^{-17}$ m$^2$ and a bedding-orthogonal permeability of $k_z = 2 \times 10^{-18}$ m$^2$. Our experiments on a cubic sample of COS also report the anisotropic permeability, although more modest, from bedding-parallel $k_x = k_y = 2.5 \times 10^{-17}$ m$^2$ to bedding-orthogonal $k_z = 1 \times 10^{-17}$ m$^2$. One advantage of UCL's TTA is its ability to measure the anisotropy of permeability using a single sample in a single experiment, thereby eliminating the effects of sample variability.

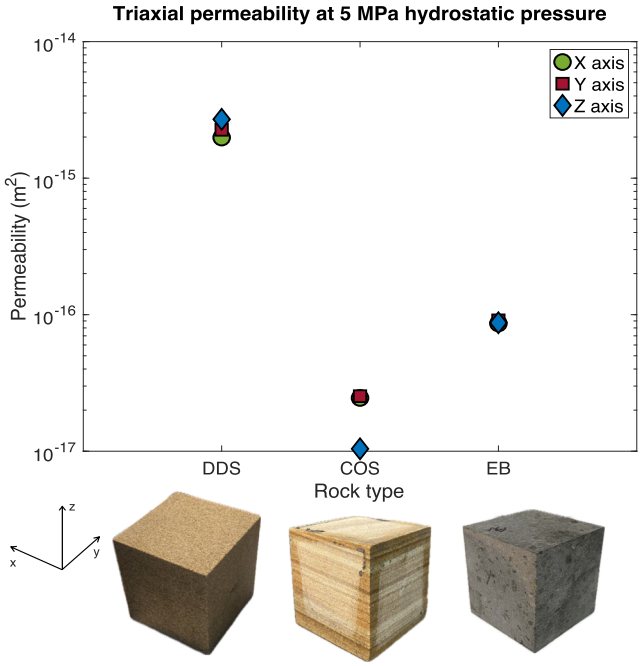


**FIG. 11.** Triaxial, hydrostatic (5 MPa) permeability of three well-known rocks: Darley Dale Sandstone (DDS), Crab Orchard Sandstone (COS), and Etna Basalt (EB).

## V. SUMMARY AND FUTURE PERSPECTIVES

We have developed a new True Triaxial Apparatus in the UCL Rock and Ice Physics Laboratory that successfully transmits independent stresses along three mutually orthogonal axes to 50 mm sided cubic samples, while accurately measuring the permeability along the three loading axes through the steady-state flow method. This apparatus will permit producing novel and much needed data on the physical and fluid flow properties of rocks subjected to truly triaxial states of stress, more representative of the natural stress conditions of the crust, and results of triaxial stress control on permeability anisotropy.

We have also explored configurations and experimental protocols that can reduce the loading boundary effects during true triaxial loading through the implementation of a suite of FEM models. We conclude that the selection of the platen material influences the end friction effect. In particular, a material that resembles the elastic properties of the rock sample ($E_{platen}/E_{rock} = 2.1$ for aluminum and sandstone) effectively reduces the extent of the end friction effect with respect to steel ($E_{platen}/E_{rock} = 5.9$) by achieving a considerably more homogeneous stress distribution. In addition, we have quantified the effect that confining pressure exerts on reducing the stress concentrations produced by unstressed edges, finding that a confining pressure of 20 MPa virtually eliminates the tensile stresses on the sample corners for the loading conditions considered in our models. We expect that these results will contribute toward developing protocols to standardize the procedures during true triaxial testing, to improve the repeatability of TTA data and expand the development of the method.

## ACKNOWLEDGMENTS

This research was financially supported by the NERC Grant Nos. NE/N007826/1 and NE/T00780X/1.

## AUTHOR DECLARATIONS

### Conflict of Interest

The authors have no conflicts to disclose.

### Author Contributions

**Ashley Stanton-Yonge**: Conceptualization (equal); Data curation (lead); Formal analysis (lead); Investigation (lead); Methodology (lead); Software (lead); Validation (lead); Visualization (lead); Writing – original draft (lead). **Thomas M. Mitchell**: Conceptualization (lead); Funding acquisition (lead); Investigation (equal); Methodology (equal); Project administration (lead); Resources (lead); Supervision (lead); Validation (equal); Visualization (supporting); Writing – review & editing (equal). **Philip G. Meredith**: Conceptualization (lead); Funding acquisition (equal); Project administration (equal); Resources (equal); Supervision (equal); Writing – review & editing (equal). **Neil Hughes**: Conceptualization (supporting); Investigation (equal); Methodology (equal); Visualization (equal). **Steve Boon**: Conceptualization (equal); Investigation (equal); Methodology (equal). **John Browning**: Conceptualization (supporting); Investigation (equal); Methodology (equal); Writing – review & editing (equal). **David Healy**: Conceptualization (supporting); Funding acquisition (equal); Project administration (equal); Resources (equal); Supervision (equal); Writing – review & editing (equal). **John Bowles**: Conceptualization (supporting); Investigation (equal); Methodology (equal).

## DATA AVAILABILITY

The data that support the findings of this study are openly available at https://doi.org/10.5281/zenodo.15167236.

## REFERENCES


Alexeev, A. D., Revva, V. N., Alyshev, N. A., and Zhitlyonok, D. M., "True triaxial loading apparatus and its application to coal outburst prediction," Int. J. Coal Geol. **58**(4), 245–250 (2004).

Atkinson, R. H. and Ko, H.-Y., "A fluid cushion, multiaxial cell for testing cubical rock specimens," Int. J. Rock Mech. Min. Sci. Geomech. Abstr. **10**, 351–354 (1973).

Balla, A., "Stress conditions in triaxial compression," J. Soil Mech. Found. Div. **86**(6), 57–84 (1960).

Boker, R., "Die mechanik der bleibenden formanderung in kristallinisch aufgebauten korpern," Verh. Dtsch. Ing. Mitt. Forsch. **175**, 1–51 (1915).

Browning, J., Meredith, P. G., Stuart, C. E., Healy, D., Harland, S., and Mitchell, T. M., "Acoustic characterization of crack damage evolution in sandstone deformed under conventional and true triaxial loading," J. Geophys. Res.: Solid Earth **122**(6), 4395–4412, https://doi.org/10.1002/2016jb013646 (2017).

Browning, J., Meredith, P. G., Stuart, C., Harland, S., Healy, D., and Mitchell, T. M., "A directional crack damage memory effect in sandstone under true triaxial loading," Geophys. Res. Lett. **45**(14), 6878–6886, https://doi.org/10.1029/2018gl078207 (2018).

Cheon, D. S., Jeon, S., Park, C., and Ryu, C., "An experimental study on the brittle failure under true triaxial conditions," Tunnelling Underground Space Technol. **21**(3–4), 448–449 (2006).

Esaki, T. and Kimura, T., "Mechanical behavior of rocks under generalized high stress conditions," in *ISRM International Symposium* (ISRM, 1989).

Feng, X.-T., Haimson, B., Li, X., Chang, C., Ma, X., Zhang, X., Ingraham, M., and Suzuki, K., "ISRM suggested method: Determining deformation and failure characteristics of rocks subjected to true triaxial compression," Rock Mech. Rock Eng. **52**, 2011–2020 (2019).

Feng, X.-T., Zhang, X., Kong, R., and Wang, G., "A novel Mogi type true triaxial testing apparatus and its use to obtain complete stress–strain curves of hard rocks," Rock Mech. Rock Eng. **49**, 1649–1662 (2016).

Feng, X.-T., Zhang, X., Yang, C., Kong, R., Liu, X., and Peng, S., "Evaluation and reduction of the end friction effect in true triaxial tests on hard rocks," Int. J. Rock Mech. Min. Sci. **97**, 144–148 (2017).

Filon, L. N. G., "IV. On the elastic equilibrium of circular cylinders under certain practical systems of load," Philos. Trans. R. Soc. London, Ser. A **198**(300–311), 147–233 (1902).

Frash, L. P., Gutierrez, M., and Hampton, J., "True-triaxial apparatus for simulation of hydraulically fractured multi-borehole hot dry rock reservoirs," Int. J. Rock Mech. Min. Sci. **70**, 496–506 (2014).

Furuzumi, M. and Sugimoto, F., "Effect of intermediate principal stress on failure of rocks and failure condition of rocks under multiaxial stresses," J. Jpn. Soc. Eng. Geol. **27**(1), 13–20 (1986).

Gehne, S. and Benson, P. M., "Permeability and permeability anisotropy in crab orchard sandstone: Experimental insights into spatio-temporal effects," Tectonophysics **712–713**, 589–599 (2017).

Golding, N., "Compressive shear faulting in ice loaded triaxially: The influence of confinement," Ph.D. thesis, Dartmouth College, 2012.

Haimson, B. and Chang, C., "A new true triaxial cell for testing mechanical properties of rock, and its use to determine rock strength and deformability of westerly granite," Int. J. Rock Mech. Min. Sci. **37**(1–2), 285–296 (2000).

Handin, J., Heard, H. C., and Magouirk, J. N., "Effects of the intermediate principal stress on the failure of limestone, dolomite, and glass at different temperatures and strain rates," J. Geophys. Res. **72**(2), 611–640, https://doi.org/10.1029/jz072i002p00611 (1967).

Hawkes, I. and Mellor, M., "Uniaxial testing in rock mechanics laboratories," Eng. Geol. **4**(3), 179–285 (1970).

He, M. C., Miao, J. L., and Feng, J. L., "Rock burst process of limestone and its acoustic emission characteristics under true-triaxial unloading conditions," Int. J. Rock Mech. Min. Sci. **47**(2), 286–298 (2010).

Huang, B., Liu, C., Fu, J., and Guan, H., "Hydraulic fracturing after water pressure control blasting for increased fracturing," Int. J. Rock Mech. Min. Sci. **48**(6), 976–983 (2011).

Kármán, T. V., "Festigkeitsversuche unter allseitigem drunk," Z. Ver. Deu. Ing. **55**, 1749 (1911).

Kern, H., "Measuring and modeling of p- and s-wave velocities on crustal rocks: A key for the interpretation of seismic reflection and refraction data," Int. J. Geophys. **2011**(1), 530728.

King, M. S., Shakeel, A., and Chaudhry, N. A., "Acoustic wave propagation and permeability in sandstones with systems of aligned cracks," Geol. Soc., London, Spec. Publ. **122**(1), 69–85 (1997).

Kwaśniewski, M., "Mechanical behavior of rocks under true triaxial compression conditions—A review," in *True Triaxial Testing of Rocks* (CRC Press, 2012), Vol. 4, p. 99.

Li, X., Shi, L., Bai, B., Li, Q., Xu, D., Feng, X. *et al.*, "True-triaxial testing techniques for rocks—State of the art and future perspectives," in *True Triaxial Testing of Rocks* (CRC Press, 2012), Vol. 4, p. 1.

Lombos, L., Roberts, D., and King, M., "Design and development of integrated true triaxial rock testing system," in *True Triaxial Testing of Rocks* (CRC Press, 2012), Vol. 4, p. 35.

Michelis, P., "A true triaxial cell for soil and rock," in *Advanced Triaxial Testing of Soil and Rock* (ASTM International, 1988).

Mogi, K., "Some presice measurements of fracture strength of rocks under uniform compressive stress," Felsmech. Ingenieurgeol. **4**(1), 41 (1966).

Mogi, K., "Effect of the intermediate principal stress on rock failure," J. Geophys. Res. **72**(20), 5117–5131, https://doi.org/10.1029/jz072i020p05117 (1967).

Mogi, K., "Effect of the triaxial stress system on the failure of dolomite and limestone," Tectonophysics **11**(2), 111–127 (1971).

Mogi, K., *Experimental Rock Mechanics* (CRC Press, 2006).

Muñoz-Ibáñez, A., Delgado-Martín, J., Juncosa-Rivera, R., Romera-Rodríguez, L., Alejano-Monge, L., Canal-Vila, J., González-Molano, N., Alvarellos-Iglesias, J., López-Puiggene, E., and Lakshmikantha, M., "Development of a true triaxial device for hydraulic fracturing experiments," in *ISRM Congress* (ISRM, 2019).

Murrell, S. A. F., "The effect of triaxial stress systems on the strength of rocks at atmospheric temperatures," Geophys. J. Int. **10**(3), 231–281 (1965).

Paterson, M. S. and Wong, T.-f., *Experimental Rock Deformation: The Brittle Field* (Springer, 2005), Vol. 348.

Rashed, G. and Peng, S. S., "Change of the mode of failure by interface friction and width-to-height ratio of coal specimens," J. Rock Mech. Geotech. Eng. **7**(3), 256–265 (2015).

Rukhaiyar, S. and Samadhiya, N. K., "Strength behaviour of sandstone subjected to polyaxial state of stress," Int. J. Min. Sci. Technol. **27**(6), 889–897 (2017).

Shi, L., Li, X., Bai, B., Li, Q., Feng, X. *et al.*, "Numerical analysis of loading boundary effects in Mogi-type true triaxial tests," in *True Triaxial Testing of Rocks* (CRC Press, 2012), Vol. 4, Issue 1, pp. 19–32.

Shi, L., Li, X., Bing, B., Wang, A., Zeng, Z., and He, H., "A Mogi-type true triaxial testing apparatus for rocks with two moveable frames in horizontal layout for providing orthogonal loads," Geotech. Test. J. **40**(4), 542–558 (2017).

Sibai, M., Henry, J. P., and Gros, J. C., "Hydraulic fracturing stress measurement using a true triaxial apparatus," Int. J. Rock Mech. Min. Sci. **34**(3–4), 289.e1 (1997).

Skoczylas, F. and Henry, J., "A study of the intrinsic permeability of granite to gas," Int. J. Rock Mech. Min. Sci. Geomech. Abstr. **8**, 376A (1995).

Smart, B. G. D., "A true triaxial cell for testing cylindrical rock specimens," Int. J. Rock Mech. Min. Sci. Geomech. Abstr. **32**, 269–275 (1995).

Spetzler, H. A., Sobolev, G. A., Sondergeld, C. H., Salov, B. G., Getting, I. C., and Koltsov, A., "Surface deformation, crack formation, and acoustic velocity changes in pyrophyllite under polyaxial loading," J. Geophys. Res.: Solid Earth **86**(B2), 1070–1080, https://doi.org/10.1029/jb086ib02p01070 (1981).

Takahashi, M. and Koide, H., "Effect of the intermediate principal stress on strength and deformation behavior of sedimentary rocks at the depth shallower than 2000 m," in *ISRM International Symposium* (ISRM, 1989).

Takahashi, M., Narita, T., Tomishima, Y., and Arai, R., "Various loading systems for rock true triaxial compression test," J. Jpn. Soc. Eng. Geol. **42**(4), 242–247 (2001).

Tiwari, R. P. and Rao, K. S., "Physical modeling of a rock mass under a true triaxial stress state," Int. J. Rock Mech. Min. Sci. **41**, 396–401 (2004).

Tshibangu, J. and Descamps, F., "The FPMS (UMons-Belgium) device for investigating the mechanical behavior of materials subjected to true triaxial compression," in *True Triaxial Testing of Rocks* (CRC Press, 2012), pp. 51–60.

Vinciguerra, S., Trovato, C., Meredith, P. G., and Benson, P. M., "Relating seismic velocities, thermal cracking and permeability in Mt. Etna and Iceland basalts," Int. J. Rock Mech. Min. Sci. **42**(7–8), 900–910 (2005).

Wawersik, W. R., Carlson, L. W., Holcomb, D. J., and Williams, R. J., "New method for true-triaxial rock testing," Int. J. Rock Mech. Min. Sci. **34**(3–4), 330.e1 (1997).

Xie, H., Lu, J., Li, C., Li, M., and Gao, M., "Experimental study on the mechanical and failure behaviors of deep rock subjected to true triaxial stress: A review," Int. J. Min. Sci. Technol. **32**(5), 915–950 (2022).

Zheng, Z., Xu, H., Zhang, K., Feng, G., Zhang, Q., and Zhao, Y., "Intermittent disturbance mechanical behavior and fractional deterioration mechanical model of rock under complex true triaxial stress paths," Int. J. Min. Sci. Technol. **34**(1), 117–136 (2024).

Zhu, W. and Wong, T.-f., "The transition from brittle faulting to cataclastic flow: Permeability evolution," J. Geophys. Res.: Solid Earth **102**(B2), 3027–3041, https://doi.org/10.1029/96jb03282 (1997).

Zoback, M. D., Barton, C. A., Brudy, M., Castillo, D. A., Finkbeiner, T., Grollimund, B. R., Moos, D. B., Peska, P., Ward, C. D., and Wiprut, D. J., "Determination of stress orientation and magnitude in deep wells," Int. J. Rock Mech. Min. Sci. **40**(7–8), 1049–1076 (2003).